

Efficient Mixed-Cation Mixed-Halide Perovskite Solar Cells by All-Vacuum Sequential Deposition Using Metal Oxide Electron Transport Layer

Matthew Kam, Yiyi Zhu, Daquan Zhang, Leilei Gu, Jiaqi Chen, and Zhiyong Fan*

The incorporation of various cations and halides to form mixed perovskites has enabled perovskite solar cells (PSCs) to exceed 20% power conversion efficiencies (PCEs). However, they are primarily prepared by solution methods, which limit film uniformity and scalability. Although co-evaporation is used to prepare all-vacuum-deposited PSCs with a decent performance, it involves multiple sources and quartz crystal monitors (QCMs) to simultaneously control deposition rates and film thicknesses, which increase production cost and fabrication complexity and interfere QCMs' reading precision. Herein, a simple and cost-effective sequential vapor deposition involving only one QCM and two sources is demonstrated as an advantageous and reliable method to fabricate high-quality and uniform mixed-cation mixed-halide perovskite films with microscale grain sizes and extraordinary morphology for the PSC application. In addition, for the first time, radio frequency (RF)-sputtered SnO₂ is implemented into all-vacuum-deposited PSCs as an electron transport layer (ETL). Together with evaporated copper phthalocyanine (CuPc) as a thermally and chemically stable low-cost hole transport layer (HTL), alternative to the commonly used 2,2',7,7'-tetrakis(*N,N*-di-*p*-methoxyphenylamino)-9,9'-spirobifluorene (Spiro-OMeTAD), which is costly, highly hygroscopic, and deliquescent, a respectable PCE of 15.14% is achieved with a promising device stability and negligible hysteresis.

1. Introduction

Organometallic halide perovskites have gained enormous attention in both academic research and photovoltaic industry over the past few years due to their highly attractive optoelectronic properties for next-generation solar cells. As one of the most intensively researched types of solar cells, perovskite solar cells (PSCs) have been rapidly developed with unprecedented

success, leading to an incredible improvement on power conversion efficiency (PCE) from 3.8% to 23.3% within a decade.^[1,2] One enchanting property of perovskites is their structural versatility to incorporate different cations and anions to form mixed perovskites, which result in a change in physical and chemical properties, such as crystal structures, bandgaps, phase stabilities, morphology, and improved moisture and/or thermal resistance.^[3–6] To date, compositional engineering of perovskites has relied on solution methods, which limit film uniformity and scalability.^[7–10] In reality, due to its excellent scalability, controllability, and high precision of film thickness detection, vapor phase vacuum deposition has been widely adopted in the photovoltaic industry for thin-film solar module fabrication with amorphous silicon, cadmium telluride, and copper indium gallium selenide (CIGS).^[11–13] In fact, in today's photovoltaic industry, when fabricating large-scale thin-film solar modules using materials, such as CdS/CdTe, CIGS, and amorphous-Si, an accurate and precise

device patterning on a large glass substrate followed by a highly controllable and uniform vacuum vapor deposition, rather than a poorly controllable solution method, provides a major advantage to effectively increase the voltage output of a large-scale PSC by electrically connecting multiple PSCs in series, thus further boosting the overall PCE. This is another reason why vacuum vapor deposition outweighs solution processing. However, a full vacuum vapor deposition approach for perovskite solar cell fabrication has seldom been explored, and it is in urgent need to enable a fast upscaling of perovskite photovoltaic for future commercialization using the existing production power for aforementioned thin-film technologies.

To date, most of the reported all-vacuum-deposited PSCs used C₆₀ as the electron transport layer (ETL) coupled with n-doped organic material, such as N¹,N⁴-bis(tri-*p*-tolylphosphoranylidene)benzene-1,4-diamine (PhIm), to improve ohmic contact. Likewise, hole transport layer (HTL) in a double-layer structure is also common in all-vacuum-deposited PSCs, for example, 4,4'-cyclohexylidenebis[*N,N*-bis(4-methylphenyl)benzenamine] (TAPC) typically couples with TAPC:MoO₃, whereas N⁴,N⁴,N⁴''

M. Kam, Y. Zhu, D. Zhang, Dr. L. Gu, Dr. J. Chen, Prof. Z. Fan
HKUST-Shenzhen Research Institute
No. 9 Yuexing first RD, South Area, Hi-tech Park, Nanshan, Shenzhen
518057, China
E-mail: eezfan@ust.hk

M. Kam, Y. Zhu, D. Zhang, Dr. L. Gu, Dr. J. Chen, Prof. Z. Fan
Department of Electronic and Computer Engineering
Hong Kong University of Science and Technology (HKUST)
Clear Water Bay, Kowloon, Hong Kong, SAR, China

 The ORCID identification number(s) for the author(s) of this article can be found under <https://doi.org/10.1002/solr.201900050>.

DOI: 10.1002/solr.201900050

$N^{4''}$ -tetra([1,1'-biphenyl]-4-yl)-[1,1':4',1''-terphenyl]-4,4''-diamine (TaTm) usually couples with 2,2'-(perfluoronaphthalene-2,6-diylidene) dimalononitrile (F_6 -TCNNQ).^[14–17] The use of a multiple-layer structure in ETL and HTL not only increases production cost, but also introduces adverse complexity and poses challenges on variation control. On the other hand, co-evaporation of mixed-perovskite films typically involves two to four quartz crystal monitors (QCMs) to simultaneously monitor the deposition status of multiple precursors, which are individually placed in crucibles.^[14,17,18] However, co-evaporation can easily trigger interference to QCMs' readings such that detected film thicknesses often drastically fluctuate. As a consequence, thickness and deposition rate are often overestimated or underestimated, ultimately compromising the film quality, which are crucial to device performance and light harvesting efficiency.^[19,20] Again, the use of multiple QCMs increases production cost and equipment complexity. Herein, we propose a simplified but powerful, novel, and cost-effective sequential vapor deposition procedure using only one QCM and two crucibles to fabricate high-quality and uniform mixed-cation mixed-halide perovskite films of the type $MA_y FA_{1-y} PbI_x Br_{3-x}$ with microscale grain sizes and desirable morphology. More importantly, a high-quality vapor-deposited perovskite film is meaningless in a device without vapor-deposited and stable ETL and HTL. Considering these requirements, it is a surprise that there is nearly no report to date on applying the radio frequency (RF)-sputtered inorganic intrinsic SnO_2 film, which is well known for its chemical, thermal, and photo-stabilities, to all-vacuum-deposited PSCs. This might be due to the technical difficulties and apprehension associated with optimizing sputtering parameters, including film thickness, sputtering working pressure, gas flow rate, and sputtering power. Therefore, mixed perovskites were implemented together with RF-sputtered SnO_2 into all-vacuum-deposited PSCs in a simple planar $n-i-p$ structure for the first time. Combining vapor-deposited low-cost copper phthalocyanine (CuPc) as the HTL with high thermal and chemical stabilities,^[21,22] the entire device can be fabricated in a single vacuum process, which is particularly attractive for commercialization. The champion device yielded a maximum PCE of 15.14% with negligible hysteresis and retained 85% of its initial PCE after 240 h exposure in air of 40% humidity.

2. Results and Discussion

The fabrication procedure of all-vacuum-deposited planar PSCs is shown in **Figure 1**. A SnO_2 film as the ETL was first sputtered at room temperature on a fluorine-doped tin oxide (FTO) glass substrate. The mixed-cation mixed-halide perovskite film was then prepared by sequential vapor deposition of lead halides followed by organic iodides with in situ annealing at 130 °C. Next, a CuPc film as the HTL and a gold film as the electrode were thermally evaporated sequentially to complete the device. It is noteworthy that both ETL and HTL are in a single-layered structure.

The full UV photoelectron spectroscopy (UPS) spectrum of sputtered SnO_2 is shown in **Figure 2a**. The sputtered SnO_2 film showed a secondary cutoff edge of 5.01 eV (Figure S1a, Supporting Information), indicating a work function W_s of 5.01 eV. Figure S1b, Supporting Information, shows that the valence band maximum (VBM) of the sputtered SnO_2 film is located at 3.07 eV, below the Fermi level E_F . The bandgap of the sputtered SnO_2 film acquired from the Tauc plot (Figure 2b) was 3.72 eV. Such a wide bandgap enhances hole blocking ability and can avoid absorption of high-energy photons, which leads to small current loss.^[23] Based on the aforementioned values, it can be calculated using the semiconductor band structure ($E_C = W_s + VBM - E_g$) that E_C of the sputtered SnO_2 film was 4.36 eV. X-ray diffraction (XRD) (Figure 2c) revealed that the sputtered SnO_2 was polycrystalline. All XRD peaks for SnO_2 were indexable to the tetragonal SnO_2 structure, indicating the formation of pure SnO_2 crystals. In addition, the sputtered SnO_2 film on FTO glass showed high transmittance close to 90% in the visible region (Figure 2d), which is slightly higher than the high-temperature-processed spin-coated SnO_2 film.^[24] These measurements convince that the room-temperature-sputtered SnO_2 has desirable properties as an effective ETL.

Co-evaporation of mixed perovskites requires multiple QCMs, control panels, and shutters to simultaneously manipulate and monitor the entire deposition process of the corresponding precursors. Apart from causing inconspicuous interference to QCMs' readings and eventually film quality, especially when precursors of similar physical properties are being evaporated simultaneously, it significantly increases the fabrication complexity and production cost. To solve this problem, sequential vapor

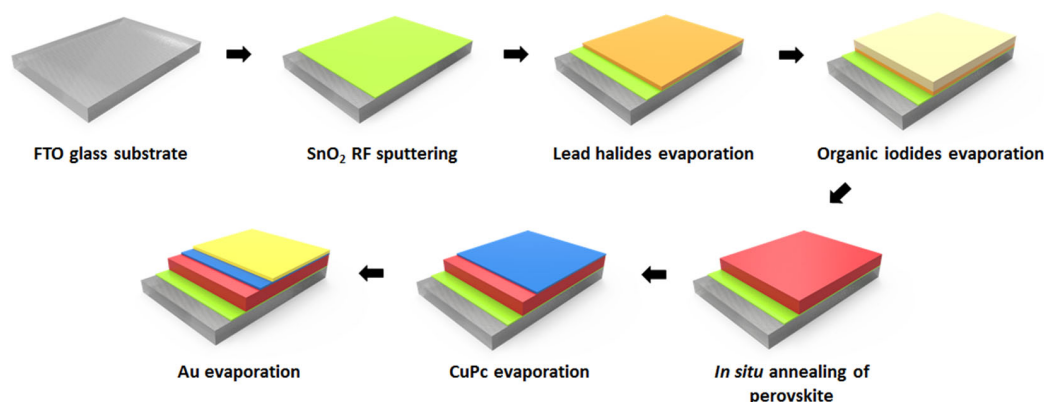


Figure 1. Schematic illustration of the fabrication procedure of an all-vacuum-deposited perovskite solar cell by sequential vapor deposition.

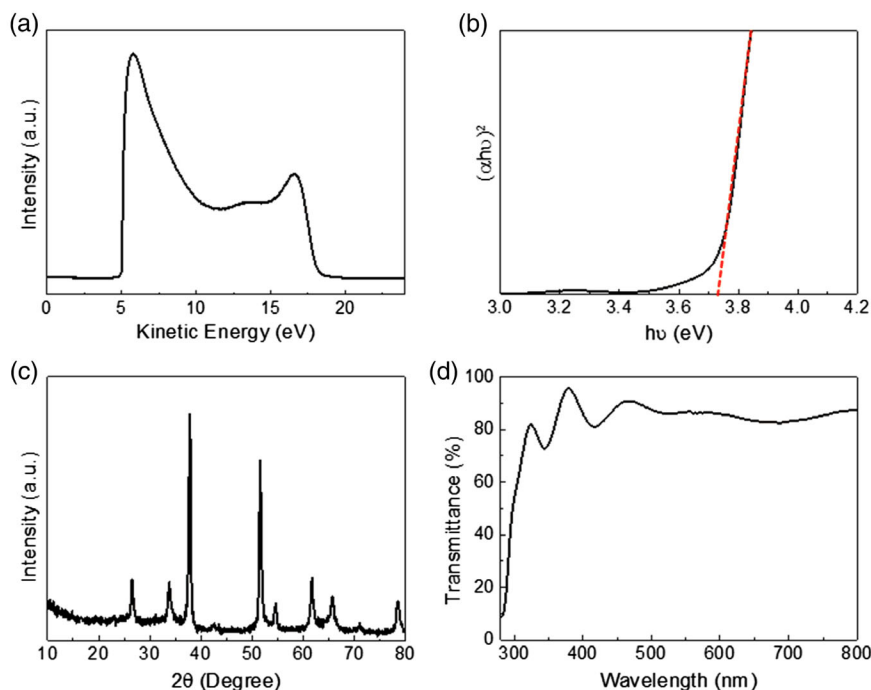


Figure 2. Thin-film characterization. a) UPS, b) Tauc plot, c) XRD, and d) transmittance of the sputtered film.

deposition comes in and is capable of acquiring high-quality and uniform perovskite films for high-performance devices.^[16,17,25,26] In reality, sequential deposition can be readily implemented in a large scale using an in-line process flow.

In this work, lead (II) iodide (PbI₂) and lead (II) bromide (PbBr₂) in an optimized ratio were mixed well simply by a stirring rod and placed in one crucible. As the boiling point of PbI₂ is just slightly higher than that of PbBr₂ and PbI₂ was the dominant precursor in the crucible, both PbI₂ and PbBr₂ can be fully evaporated effectively with a given heating current. The resultant film thickness was determined based on the density and acoustic impedance of PbI₂ after calibration of the tooling factor. On the other hand, methylammonium iodide (MAI) and formamidinium iodide (FAI) in an optimized ratio were also mixed well in the same way and placed in another crucible. No grinding of precursors was needed. As they sublime at close temperature, they can also be fully evaporated at a very similar rate. In other words, it would not be a concern that one precursor being evaporated while another remained unaffected in the crucible. As precursors in crucibles were calibrated beforehand and two crucibles of precursors were evaporated sequentially, only one QCM was required. Unlike the conventional way to fabricate mixed perovskite via only adjusting the thicknesses of the respective film, here, the ratios of precursors were optimized beforehand to ensure that the weighed precursors would be completely evaporated onto the substrates while the QCM simultaneously monitored the film deposition rate and thickness. Therefore, cleaning process after the deposition of organic iodides was not necessary. The most suitable thickness of the resultant mixed-perovskite film was calibrated to be approximately 400 nm after determining the optimized thickness ratio of lead halides to organic iodides. It was found that a too thin perovskite film weakened light

absorption and deteriorated film stability, whereas a too thick perovskite film composed of multilayers aggravated charge recombination due to finite carrier diffusion length. On the other hand, the thickness of lead halides was critical because their amount influenced the light absorption of the resultant perovskite film as excessive lead halides would significantly blueshift the absorption edge of perovskite. The thickness of organic iodides was subsequently adjusted such that all organic iodides deposited could fully react with the lead halides deposited and hence avoid the accumulation of excessive lead halides between the perovskite film and the SnO₂ layer. Lead halides (120 nm) and organic iodides (280 nm) were consequently taken as the optimized ratio.

It was reported that the conversion from tetragonal to cubic phase by doping 20% Br into MAPbI₃ demonstrated better stability against moisture.^[27] However, it was also shown that V_{oc} decreased in MAPbI_xBr_{3-x}-based devices with an increasing amount of Br when the content was over 20% due to phase segregation.^[27,28] With reference to previous studies, three ratios were attempted, and the device performances based on respective ratios were compared, as shown in Table S1, Supporting Information. It was found that a device with the PbI₂:PbBr₂ ratio of 4.65 yielded the highest PCE of 10.84%. Energy-dispersive X-ray spectroscopy (EDX) shown in Figure S2, Supporting Information, was used to determine halide composition in the mixed-halide perovskite films. The PbI₂:PbBr₂ ratio of 4.65, which corresponded to 11% Br doping, was taken as the optimum doping content. For mixed cation, it was reported that the MAI:FAI ratio of 3:2 exhibited the best photovoltaic performance and light-harvesting ability compared with other MAI:FAI ratios because of the absence of the undesirable δ -FAPbI₃ phase.^[29] With reference to this finding, device performances based on three different MAI:FAI ratios were

compared, as also shown in Table S1, Supporting Information. It was found that a device with the MAI:FAI ratio of 1.27 ($\text{MA}_{0.56}\text{FA}_{0.44}$) yielded the highest PCE of 13.71%. The methylammonium (MA) and formamidinium (FA) contents were determined from the precursor weighed ratio. Hereafter, the $\text{PbI}_2:\text{PbBr}_2$ ratio of 4.65 and the MAI:FAI ratio of 1.27 were taken as the optimized recipe for mixed-halide perovskite of the form $\text{MAPbI}_{2.67}\text{Br}_{0.33}$ and mixed-cation mixed-halide perovskite of the form $\text{MA}_{0.56}\text{FA}_{0.44}\text{PbI}_{2.67}\text{Br}_{0.33}$.

To systematically investigate the individual impact of mixed halide and mixed cation, $\text{MAPbI}_{2.67}\text{Br}_{0.33}$ and $\text{MA}_{0.56}\text{FA}_{0.44}$

$\text{PbI}_{2.67}\text{Br}_{0.33}$ films were fabricated for thin-film characterization and device performance comparison. For $\text{MAPbI}_{2.67}\text{Br}_{0.33}$, a mixture of PbI_2 and PbBr_2 was first evaporated and deposited on FTO glass substrates (Figure S3, Supporting Information), followed by MAI deposition with in situ annealing for 40 and 60 min at 130 °C (defined as MA40 and MA60, respectively). In Figure 3a–d, scanning electron microscopy (SEM) revealed that $\text{MAPbI}_{2.67}\text{Br}_{0.33}$ grain sizes slightly increased and its morphology improved as the duration of in situ annealing prolonged. However, two distinct layer structures were also observed in the cross-sectional SEM images. A thin (50–100 nm) layer of lead

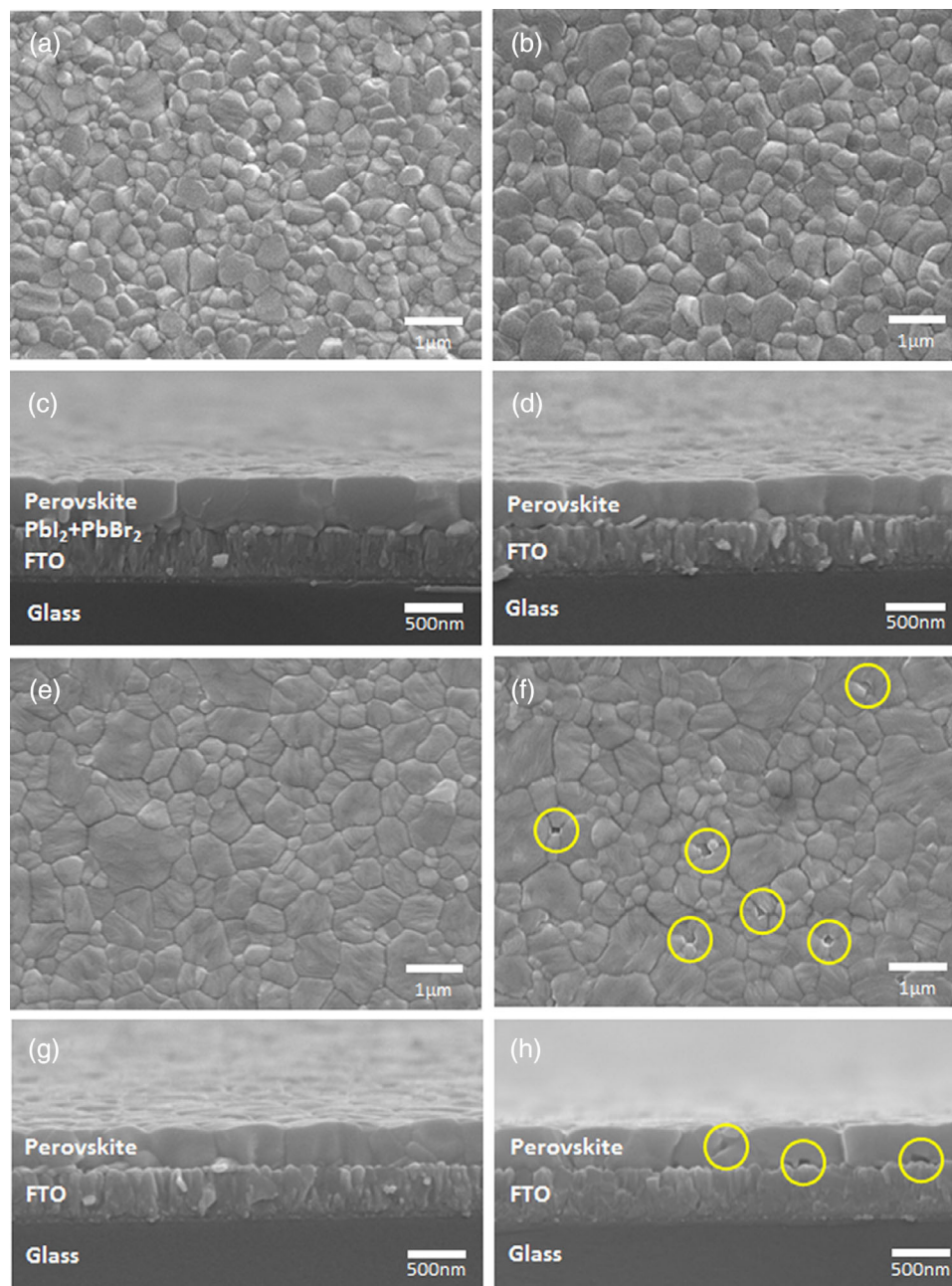


Figure 3. Top-view and cross-sectional SEM images of a,c) MA40, b,d) MA60, e,g) MAFA40, and f,h) MAFA60 sequentially deposited mixed-perovskite films on FTO glass substrates.

halides remained underneath the top of the perovskite layer in the FTO-perovskite interface of the MA40 perovskite sample, which suggested incomplete crystallization and incomplete reaction between lead halides and organic iodides. For the MA60 perovskite, prolonged annealing completed reaction and crystallization, but the grain sizes were generally not enlarged. In contrast, when FAI was vapor-deposited together with MAI, highly crystalline, uniform, smooth, and compact single-crystal-thick MA_{0.56}FA_{0.44}PbI_{2.67}Br_{0.33} perovskite films with microscale grain sizes as large as 3.5 μm were acquired, as shown in Figure 3e–h and Figure S4, Supporting Information. The MA_{0.56}FA_{0.44}PbI_{2.67}Br_{0.33} perovskite films were also annealed for 40 and 60 min (defined as MAFA40 and MAFA60, respectively). As revealed by cross-sectional SEM, the former perovskite grains were so compact such that the grain boundaries were hard to discern. Most of the grain boundaries were perpendicular to the substrate, thus minimizing the energy barrier for carrier transport from perovskite to ETL and HTL. As it underwent prolonged in situ annealing, tiny pinholes formed between grains and the FTO-perovskite interface in the MAFA60 perovskites as indicated by yellow circles, which could reduce the efficiency of carrier transport from perovskite to the ETL and HTL. However, it was possible that excessive iodide provided by MAI and FAI could gradually replace bromide as the deposition process took longer and hence affected the amount of Br doping in the resultant mixed-cation mixed-halide perovskites. EDX was performed to deduce I:Br molar ratios of a parent mixed-halide film and mixed-cation mixed-halide perovskites that underwent different annealing durations, as shown in Table S2, Supporting Information. Results showed that I:Br molar ratios in mixed perovskite increased with annealing duration because prolonged deposition of organic iodides increased the exposure of the mixed-halide film to constant supply of iodide as the dominant halide for further reaction and crystallization. As a result, the amount of Br doping of each mixed-perovskite film would be correspondingly modified.

Apparently, in situ annealing promoted in situ reaction between lead halides and organic iodides as sequential vapor deposition took place, thereby enhancing perovskite crystallization. Figure S5, Supporting Information, shows a cross-sectional SEM image of perovskite thin films without being in situ annealed. A thin layer of small perovskite grains at the top and an excessive amount of unreacted lead halides between the perovskite-FTO interfaces reflected a slow reaction between

lead halides and organic iodides in the absence of in situ annealing. Therefore, in situ annealing was essential. In fact, in situ annealing not only minimizes exposure to humidity and contamination during manual sample handling but is also convenient and time saving for a continuous flow of fabrication process for high throughput production. On the other hand, it is worth pointing out that all the aforementioned mixed perovskites as well as the final devices were fabricated on FTO glass substrates with a rougher surface than the commonly used ITO glass substrates for all-vacuum-deposition, and high-quality single-crystal-thick perovskite films could also be acquired.

The UV-visible spectroscopy (UV-vis) absorption spectra of MA40, MA60, MAFA40, and MAFA60 perovskite thin films (Figure 4a) show absorption onsets corresponding to an optical bandgap of 1.65 and 1.62 eV, respectively, estimated from the Tauc plot (Figure S6a, Supporting Information), which matched well with respective steady-state photoluminescence (PL) peaks at 752 and 763 nm (Figure S6b, Supporting Information). According to the UV-vis spectra, both MAFA40 and MAFA60 perovskite thin films demonstrated a stronger light-harvesting ability than MA40 and MA60, which was attributed to complete reaction between lead halides and organic iodides to form highly crystalline perovskite films. The films were further characterized using XRD (Figure 4b). All presented the expected perovskite pattern, with intense signals at 14.1°, 28.4°, and 31.9° corresponding to the (100), (200), and (310) crystal orientations, respectively. The MA40 perovskite film showed an XRD pattern with very weak signal intensities due to incomplete crystallization and incomplete reaction. In comparison, significantly stronger signal intensities were observed on MA60 perovskite with prolonged in situ annealing, which allowed a more complete crystallization and reaction between lead halides and organic iodides. However, it also showed an extra peak at 12.7°, indicating the presence of PbI₂, which can be attributed to perovskite deterioration into PbI₂ or incomplete conversion from lead halides into perovskite. On the other hand, the MAFA40 perovskite showed the most intense signal intensities. The absence of the characteristic absorption features and the diffraction peaks of metal halides in MAFA40 perovskite indicated a total conversion of metal halides to perovskite upon sublimation of organic halides. Similar to MA60, there was also a small diffraction peak of PbI₂ at 12.7° in MAFA60 perovskite, which implied over-annealing. In addition, the weak component at 11.5° may originate from the undesirable residual δ-phase in MA_{0.56}FA_{0.44}PbI_{2.67}Br_{0.33}.^[30]

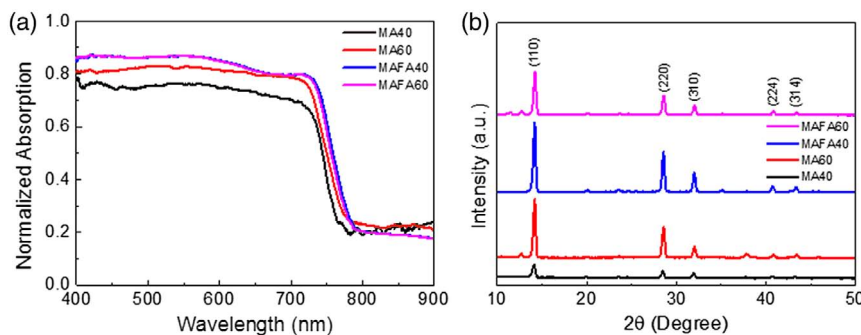


Figure 4. Mixed-perovskite thin-film characterization. a) UV-vis spectra and b) XRD patterns of MA40, MA60, MAFA40, and MAFA60 sequentially vapor-deposited mixed-perovskite films.

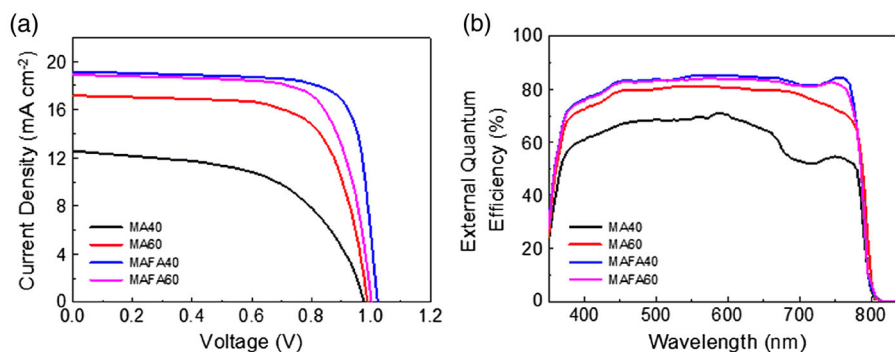


Figure 5. Device characterization. a) J - V characteristics and b) corresponding EQE spectra of PSCs using mixed-perovskite absorbers fabricated in different compositions and conditions.

Figure 5 shows the current density-to-voltage (J - V) characteristics and the corresponding external quantum efficiency (EQE) of the champion all-vacuum-deposited PSCs that employed MA40, MA60, MAFA40, and MAFA60 mixed perovskites. The device performance parameters extracted from the characterization are summarized in **Table 1**. As expected, the highest performing device was based on MA_{0.56}FA_{0.44}PbI_{2.67}Br_{0.33} with in situ annealing for 40 min (MAFA40). The cell delivered an open-circuit voltage (V_{oc}) of 1.02 V, a large short-circuit current density (J_{sc}) of 19.16 mA cm⁻², and a high fill factor (FF) of 77.3%, leading to a decent PCE of 15.14%. This result convinces that this simplified sequential vapor deposition of lead halides and organic iodides in optimized precursor weight ratios to fabricate mixed perovskite is also effective to deliver all-vacuum-deposited PSCs with competitive PCEs. The corresponding EQE also showed a curve with a value of around 80% across the entire wavelength range of 450–750 nm, indicating full absorption and efficient carrier generation in the MAFA40 perovskite film. The significant PL quench observed on the MAFA40 perovskite film deposited on sputtered SnO₂ suggests SnO₂ as an effective ETL and reinforces the high-performance device explanation (Figure S7, Supporting Information). On the other hand, the MAFA60 PSC also demonstrated a satisfactory performance. The marginal decrease in J_{sc} and FF may be attributed to the formation of pinholes between grains and the perovskite-ETL interface, which hindered charge collection and/or stimulated charge recombination within the device. The residual δ -phase due to the FA content revealed by XRD (Figure 4b) could be an indicator of phase instability and consequently compromised device performance. In contrast, the device with the MA40 perovskite absorber exhibited a substantial loss of J_{sc} and FF down to

Table 1. Respective device performance parameters based on MA40, MA60, MAFA40, and MAFA60 perovskite.

Mixed perovskite	Annealing direction [min]	V_{oc} [V]	J_{sc} [mA cm ⁻²]	FF [%]	PCE [%]
MA40	40	0.98	12.55	56.1	6.89
MA60	60	0.99	17.17	68.6	11.66
MAFA40	40	1.02	19.16	77.3	15.14
MAFA60	60	1.00	18.91	72.3	13.69

12.55 mA cm⁻² and 56.1%, respectively, resulting in a low PCE of 6.89%. It was because of the unconverted lead halides between perovskite and ETL, as clearly observed in the cross-sectional SEM image shown in Figure 3c. The insufficiently crystallized perovskite, therefore, resulted in reduced absorption and decreased EQE in the red and IR wavelength range. Allowing additional 20 min of in situ annealing enhanced the interfacial reaction between lead halides and organic iodides. The complete formation and better crystallinity of perovskite together with expanded grain sizes improve device PCE from 6.89% to 11.66% by boosting J_{sc} and FF by 37% and 22%, respectively. Nevertheless, MA60 perovskite was slightly over-annealed, causing its deterioration into PbI₂, as suggested by XRD. This was the reason why J_{sc} of MA60 PSC was lower than that of MAFA40 PSC. It was clear that the introduction of an optimized amount of FA into vapor-deposited mixed-halide perovskites not only enhanced crystallinity and morphology, enlarged grain sizes, but also demonstrated a significant improvement on FF, which altogether were the keys to achieve nearly a 30% increase in PCE. The high performance of the champion device can also be attributed to the continuous low-contamination vacuum deposition process throughout the entire device fabrication process and the continuous, homogeneous, and pinhole-free perovskite thin film.

To further understand the impact of mixed-halide and mixed-cation perovskites, hysteresis and device stability tests were carried out. As shown in **Figure 6a**, negligible hysteresis of the J - V characteristics of the champion MAFA40 PSC was observed for the reverse and forward scan directions. In contrast, there existed an evident hysteresis effect on the champion MA60 PSC. The device performance parameters extracted from the characterization are summarized in **Table 2**. Their device stabilities were also tested by leaving them unencapsulated to continuous exposure to air with 40% humidity for 240 h. **Figure 6b** shows the evolution of their normalized PCEs during the period. It was found that the MAFA40 PSC retained 85% of its initial PCE, whereas the MA60 PSC could only retain 75% of its initial PCE after 240 h. XRD was conducted to examine if any residual FA δ -phase arose in the MAFA40 PSC during the tested period and contributed to the decrease in PCE. Neither signal from PbI₂ nor FA δ -phase was detected, as shown in Figure S8, Supporting Information. It was evident that the mixed-cation mixed-halide PSCs demonstrated better device stability than mixed-halide PSCs in air.

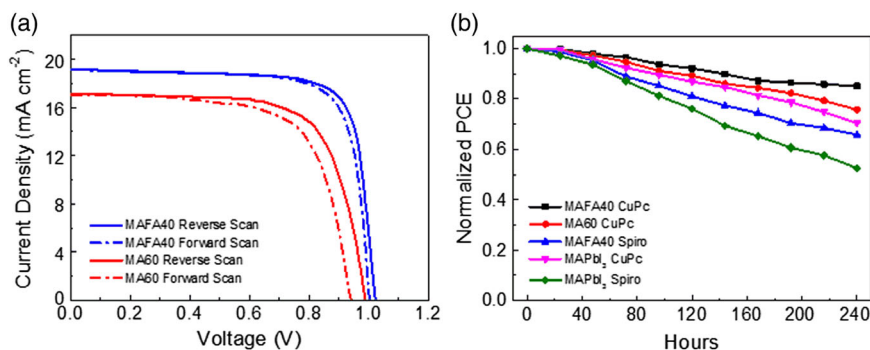


Figure 6. a) J - V characteristics of the champion devices with MAFA40 and MA60 perovskite absorbers measured under reverse and forward voltage scanning with AM1.5G illumination and b) 240 h stability test in air of 40% humidity of champion devices with MAFA40 and MA60 perovskite absorbers.

Table 2. Respective device performance and hysteresis test of device based on MA60 and MAFA40 perovskite.

Mixed perovskite	Scanning direction	V_{oc} [V]	J_{sc} [mA cm^{-2}]	FF [%]	PCE [%]
MA60	Reverse	0.99	17.17	68.6	11.66
	Forward	0.94	17.03	66.8	10.69
MAFA40	Reverse	1.02	19.16	77.3	15.14
	Forward	1.00	19.14	76.7	14.73

Furthermore, the CuPc film, which is thermally and chemically stable, could fully cover the perovskite films (Figure S4, Supporting Information) and hence inhibit the ingress of moisture and air into perovskite. Therefore, the CuPc HTL also played an important role on the device stability. To reinforce this assertion, three additional devices were fabricated, following the same optimized conditions to illustrate the ability of CuPc to protect perovskite from moisture and air ingress and prove the advantages of mixed perovskites compared with ordinary MAPbI₃ pure perovskite. Figure S9, Supporting Information, shows the J - V characteristics of the studied devices, and Table S3, Supporting Information, displays their performance parameters. Devices with 2,2',7,7'-tetrakis(*N,N*-di-*p*-methoxyphenylamino)-9,9'-spirobifluorene (Spiro-OMeTAD) as HTL yielded lower FF but higher J_{sc} , because of the addition of lithium bis(trifluoromethylsulfonyl)imide (Li-TFSI) as a p-dopant to increase conductivity and hole mobility.^[31,32] It was clear that grain sizes and morphology of pinhole-free single-crystal thick mixed-cation mixed-halide perovskites, as shown in Figure 3e, f, were generally threefold larger and smoother than those of ordinary MAPbI₃ pure perovskite with multiple grain layers, as shown in Figure S10, Supporting Information. It can be concluded that mixed-cation and mixed-halide compositions were beneficial to charge collection, reduction of carrier recombination, and film morphology. Therefore, it is reasonable that the MAPbI₃-based PSC demonstrated poorer PCE than the MAFA40-based PSC, whereas the Spiro-OMeTAD-based device showed poorer PCE than the CuPc-based device. The stability tests shown in Figure 6b revealed that the PCEs of Spiro-OMeTAD-based PSCs dropped to 66% and 53% of their initial

PCEs, whereas CuPc-based devices could retain 85%, 76%, and 70% of their respective initial PCEs after the same 240 h stability test. Such a major difference can be explained by the highly hygroscopic and deliquescent nature of Li-TFSI and the highly mobile nature of Li⁺ cations, which facilitated moisture-induced degradation.^[33] On the other hand, the highly mobile Li⁺ cations could migrate throughout the device stack during operation, unintentionally causing modification of other materials in the device stack, increasing device hysteresis, and potentially leading to redox reaction with the perovskite films.^[34,35] These results strengthened the advantages of mixed cation mixed halide and CuPc HTL to the performance and stability of PSCs.

To demonstrate the reproducibility of the sequential vacuum deposition technique, 18 separate devices from three different batches were fabricated and characterized using the optimized fabrication conditions (MAFA40 and MA60). The histogram in Figure S11, Supporting Information, shows a normal distribution of their PCEs. The average PCE of 14% achieved by MAFA40 PSCs was also encouraging, which was only slightly lower than the best PCE of 15.14%. The promising results demonstrated the great advantage of this fabrication method in the production of solar modules.

Compared with previously reported co-evaporation of perovskite layers,^[19,36–39] our simplified sequential vapor deposition possesses three distinct advantages: 1) it is highly effective and repeatable to produce high-quality, uniform, and single-crystal-thick mixed-cation mixed-halide perovskite films with microscale crystal domain size and extraordinary morphology for efficient carrier transporting and minimum recombination, even on rough FTO glass substrates; 2) the simplified fabrication procedure and infrastructure requirement are cost-effective, and they minimize the risk of contamination, mishandling, as well as QCM interference; and 3) more importantly, using vapor-deposited single-layered SnO₂ and CuPc as the highly stable ETL and HTL, respectively, together with a metal electrode, the entire device in such an elegant planar structure can be fabricated in a single vacuum process.

3. Conclusion

In summary, we have developed a simplified but powerful sequential vapor deposition technique to fabricate high-quality,

uniform, and single-crystal-thick mixed-cation mixed-halide perovskite films with microscale grain sizes for all-vacuum-deposited planar PSCs. Instead of conventionally adjusting the thickness of each precursor, the mass ratios of precursors were optimized beforehand to acquire a perovskite film in desired stoichiometry. Moreover, sputtered SnO₂ films were implemented as ETL into all-vacuum-deposited PSCs for the first time. By sandwiching these mixed-perovskite films between vapor-deposited single-layered SnO₂ and CuPc, such a planar device demonstrated a respectable performance of $V_{oc} = 1.02$ V, $J_{sc} = 19.16$ mA cm⁻², FF = 77.3%, and a decent PCE as high as 15.14%. The cell also demonstrated a promising stability and negligible hysteresis. This highly reproducible sequential vapor deposition approach not only simplifies the conventional co-evaporation of mixed perovskites but also convinces the effectiveness and compatibility of vacuum-processed metal oxides with all-vacuum-deposited PSCs. We envisage that the integration of such an elegant device structure, a simplified and cost-effective fabrication procedure, with the compatibility of a matured mass-production infrastructure will enlighten the research and industrial fields and eventually bring the perovskite photovoltaic technology a big step toward vast production.

4. Experimental Section

Materials: FTO-coated glass substrates were purchased from Zhuhai Kaivo Optoelectronic Technology Co., Ltd. The SnO₂ target of 2 in. diameter was purchased from Chinese Rare Metal Material Co., Ltd. MAI and FAI were purchased from Dyesol. PbI₂, PbBr₂, and CuPc were purchased from Sigma-Aldrich. All materials were used as received.

Device Fabrication: The substrates were sequentially washed with acetone, isopropanol, and deionized water. The sheet resistance of FTO is 15 Ω⁻¹, and the thicknesses of glass and FTO are 1.6 mm and 420 nm, respectively. The average transmittance of FTO glass in the visible region is 85%. SnO₂ was deposited on FTO glass by RF sputtering in room temperature. The clean substrates were transferred to a vacuum chamber and evacuated to a pressure of 4×10^{-4} Pa for SnO₂ sputtering. The substrates were mounted on a rotating platform, 10 cm above the SnO₂ target for sputtering. The sputtering atmosphere consisted of O₂ and Ar. When 4×10^{-4} Pa was reached, O₂ (99.99%) and Ar (99.998%) were pumped into the chamber. The gas flow rates of O₂ and Ar were controlled by gas-flow meters, and the gas flow ratio of O₂ and Ar was set at 5 and 50 sccm, respectively. The working pressure for sputtering was maintained at 0.25 Pa when the SnO₂ target was sputtered with a sputtering power of 60 W. SnO₂ (40 nm) was sputtered at a deposition rate of 0.43 Å s⁻¹. Subsequently, mixed-perovskite films were deposited on SnO₂-coated FTO glass substrates by sequential vapor deposition. The sources were located at the bottom of the chamber with an angle of 90° with respect to the substrates. The distance between the source and substrate was 20 cm. The evaporation rate of lead halides and organic iodides was maintained in a range of 1.5–2.0 Å s⁻¹. Lead halides and organic iodides of different ratios mixed together by stirring rods were tested and placed in two distinct crucibles for sequential vapor deposition. Lead halides (120 nm) and organic iodides (280 nm) were evaporated sequentially to generate mixed-perovskite films of about 400 nm. The mixed-perovskite films were in situ annealed at 130 °C for 40 or 60 min during the deposition of organic iodides. To complete the device, the perovskite films were covered by CuPc of 60 nm and gold of 100 nm, deposited sequentially by thermal evaporation both at 1.0 Å s⁻¹. For devices based on Spiro-OMeTAD as the HTL, it composed of 80 mg mL⁻¹ chlorobenzene, 17.5 μL Li-TFSI (520 mg mL⁻¹ acetonitrile), and 28.5 μL TBP. The solution was spin-coated on top of perovskite films at 3000 rpm for 30 s. The films were left in a desiccator overnight before thermal evaporation of gold.

Device Measurements: The AM1.5G solar spectrum was simulated by an Abet Class AAB Sun 2000 simulator with an intensity of 100 mW cm⁻² calibrated with a KG5-filtered Si reference cell. The current–voltage (*I*–*V*) data were measured using a 2400 series sourcemeter (Keithley, USA). *I*–*V* sweeps (forward and reverse) were performed between –1.2 and +1.2 V, with a step size of 0.02 V and a delay time of 100 ms at each point.

Material Characterization: The field-emission scanning electron microscopy (JEOL JSM-7100F) and XRD method (Bruker D8 X-ray diffractometer, USA) using Cu Kα radiation were used to study the thickness, morphology, roughness of the films, and phase characterization. The optical absorption and steady-state PL spectra were recorded on a Lambda 20 spectrophotometer (Perkin Elmer, USA) and InVia (Renishaw) micro Raman/PL system, respectively. UV photoelectron spectroscopy (Axis Ultra DLD) was used to determine the VBM of SnO₂ films.

Supporting Information

Supporting Information is available from the Wiley Online Library or from the author.

Acknowledgements

This work was supported by National Natural Science Foundation of China (Project No. 51672231), Shen Zhen Science and Technology Innovation Commission (Project No. JCYJ20170818114107730), and Hong Kong Research Grant Council (General Research Fund Project No. 16237816). The authors also acknowledge the support from the Center for 1D/2D Quantum Materials and the State Key Laboratory on Advanced Displays and Optoelectronics at HKUST.

Conflict of Interest

The authors declare no conflict of interest.

Keywords

all-vacuum-deposited perovskite solar cells, cost-effective commercialization, mixed-cation mixed-halide perovskite, sequential vapor deposition, SnO₂

Received: February 2, 2019

Revised: March 27, 2019

Published online:

- [1] A. Kojima, K. Teshima, Y. Shirai, T. Miyasaka, *J. Am. Chem. Soc.* **2009**, *131*, 6050.
- [2] NREL, Efficiency chart, <https://www.nrel.gov/pv/assets/images/efficiency-chart-20180716.jpg> (accessed: June **2018**).
- [3] J. Xiao, L. Liu, D. Zhang, N. De Marco, J. Lee, O. Lin, Q. Chen, Y. Yang, *Adv. Energy Mater.* **2017**, *7*, 1700491.
- [4] Y. Zhou, Z. Zhou, M. Chen, Y. Zong, J. Huang, S. Pang, N. P. Padture, *J. Mater. Chem. A* **2016**, *4*, 17623.
- [5] J. Albero, A. M. Asiri, H. García, *J. Mater. Chem. A* **2016**, *4*, 4353.
- [6] Z. Wang, Z. Shi, T. Li, Y. Chen, W. Huang, *Angew. Chem., Int. Ed.* **2017**, *56*, 1190.
- [7] N. J. Jeon, J. H. Noh, W. S. Yang, Y. C. Kim, S. Ryu, J. Seo, S. I. Seok, *Nature* **2015**, *517*, 476.
- [8] M. Saliba, T. Matsui, K. Domanski, J. Y. Seo, A. Ummadisingu, S. M. Zakeeruddin, J. P. Correa-Baena, W. R. Tress, A. Abate, A. Hagfeldt, M. Gratzel, *Science* **2016**, *354*, 206.

- [9] S. Albrecht, M. Saliba, J. P. C. Baena, F. Lang, L. Kegelmann, M. Mews, L. Steier, A. Abate, J. Rappich, L. Korte, *Energy Environ. Sci.* **2016**, *9*, 81.
- [10] N. J. Jeon, J. H. Noh, Y. C. Kim, W. S. Yang, S. Ryu, S. I. Seok, *Nat. Mater.* **2014**, *13*, 897.
- [11] R. Miles, *Vacuum* **2006**, *80*, 1090.
- [12] K. W. Mitchell, A. L. Fahrenbruch, R. H. Bube, *J. Appl. Phys.* **1977**, *48*, 4365.
- [13] K. Ramanathan, M. A. Contreras, C. L. Perkins, S. Asher, F. S. Hasoon, J. Keane, D. Young, M. Romero, W. Metzger, R. Noufi, *Prog. Photovoltaics: Res. Appl.* **2003**, *11*, 225.
- [14] G. Longo, C. Momblona, M. La-Placa, L. Gil-Escrig, M. Sessolo, H. J. Bolink, *ACS Energy Lett.* **2018**, *3*, 214.
- [15] L. Gil-Escrig, C. Momblona, M. La-Placa, P. P. Boix, M. Sessolo, H. J. Bolink, *Adv. Energy Mater.* **2018**, *8*, 1703506.
- [16] S. Hsiao, H. Lin, W. Lee, W. Tsai, K. Chiang, W. Liao, C. Ren-Wu, C. Chen, H. Lin, *Adv. Mater.* **2016**, *28*, 7013.
- [17] C. Chen, H. Lin, K. Chiang, W. Tsai, Y. Huang, C. Tsao, H. Lin, *Adv. Mater.* **2017**, *29*, 1605290.
- [18] X. Zhu, D. Yang, R. Yang, B. Yang, Z. Yang, X. Ren, J. Zhang, J. Niu, J. Feng, S. F. Liu, *Nanoscale* **2017**, *9*, 12316.
- [19] C. Chen, H. Kang, S. Hsiao, P. Yang, K. Chiang, H. Lin, *Adv. Mater.* **2014**, *26*, 6647.
- [20] L. K. Ono, S. Wang, Y. Kato, S. R. Raga, Y. Qi, *Energy Environ. Sci.* **2014**, *7*, 3989.
- [21] Y. Kim, T. Yang, N. Jeon, J. Im, S. Jang, T. Shin, H. Shin, S. Kim, E. Lee, J. Noh, *Energy Environ. Sci.* **2017**, *10*, 2109.
- [22] F. Zhang, X. Yang, M. Cheng, W. Wang, L. Sun, *Nano Energy* **2016**, *20*, 108.
- [23] W. Ke, G. Fang, Q. Liu, L. Xiong, P. Qin, H. Tao, J. Wang, H. Lei, B. Li, J. Wan, *J. Am. Chem. Soc.* **2015**, *137*, 6730.
- [24] H. Yu, H. Yeom, J. W. Lee, K. Lee, D. Hwang, J. Yun, J. Ryu, J. Lee, S. Bae, S. K. Kim, *Adv. Mater.* **2018**, *30*, 1704825.
- [25] M. M. Tavakoli, K. Tsui, Q. Zhang, J. He, Y. Yao, D. Li, Z. Fan, *ACS Nano* **2015**, *9*, 10287.
- [26] M. M. Tavakoli, Q. Lin, S. Leung, G. C. Lui, H. Lu, L. Li, B. Xiang, Z. Fan, *Nanoscale* **2016**, *8*, 4276.
- [27] J. H. Noh, S. H. Im, J. H. Heo, T. N. Mandal, S. I. Seok, *Nano Lett.* **2013**, *13*, 1764.
- [28] D. J. Slotcavage, H. I. Karunadasa, M. D. McGehee, *ACS Energy Lett.* **2016**, *1*, 1199.
- [29] N. Pellet, P. Gao, G. Gregori, T. Yang, M. K. Nazeeruddin, J. Maier, M. Grätzel, *Angew. Chem.* **2014**, *126*, 3215.
- [30] A. Binek, F. C. Hanusch, P. Docampo, T. Bein, *J. Phys. Chem. Lett.* **2015**, *6*, 1249.
- [31] S. Wang, W. Yuan, Y. S. Meng, *ACS Appl. Mater. Interfaces* **2015**, *7*, 24791.
- [32] A. Abate, T. Leijtens, S. Pathak, J. Teuscher, R. Avolio, M. E. Errico, J. Kirkpatrick, J. M. Ball, P. Docampo, I. McPherson, *Phys. Chem. Chem. Phys.* **2013**, *15*, 2572.
- [33] T. Leijtens, T. Giovenzana, S. N. Habisreutinger, J. S. Tinkham, N. K. Noel, B. A. Kamino, G. Sadoughi, A. Sellinger, H. J. Snaith, *ACS Appl. Mater. Interfaces* **2016**, *8*, 5981.
- [34] Z. Li, C. Xiao, Y. Yang, S. P. Harvey, D. H. Kim, J. A. Christians, M. Yang, P. Schulz, S. U. Nanayakkara, C. Jiang, *Energy Environ. Sci.* **2017**, *10*, 1234.
- [35] J. A. Dawson, A. J. Naylor, C. Eames, M. Roberts, W. Zhang, H. J. Snaith, P. G. Bruce, M. S. Islam, *ACS Energy Lett.* **2017**, *2*, 1818.
- [36] C. Roldán-Carmona, O. Malinkiewicz, A. Soriano, G. M. Espallargas, A. Garcia, P. Reinecke, T. Kroyer, M. I. Dar, M. K. Nazeeruddin, H. J. Bolink, *Energy Environ. Sci.* **2014**, *7*, 994.
- [37] O. Malinkiewicz, A. Yella, Y. H. Lee, G. M. Espallargas, M. Graetzel, M. K. Nazeeruddin, H. J. Bolink, *Nat. Photonics* **2014**, *8*, 128.
- [38] H. Hu, D. Wang, Y. Zhou, J. Zhang, S. Lv, S. Pang, X. Chen, Z. Liu, N. P. Padture, G. Cui, *RSC Adv.* **2014**, *4*, 28964.
- [39] A. Ng, Z. Ren, Q. Shen, S. H. Cheung, H. C. Gokkaya, G. Bai, J. Wang, L. Yang, S. K. So, A. B. Djurišić, *J. Mater. Chem. A* **2015**, *3*, 9223.